Link to glow - iEDDA conjugation of a Ruthenium(II) tetrazine complex leading to dihydropyrazine and pyrazine complexes with improved $^1O_2$ formation ability

Carolin Müller [a,b,§], Pascal Wintergerst [c,§], Shruthi Santhosh Nair [a,b,§], Nicolas Meitinger [c], Sven Rau [c,*], Benjamin Dietzek-Ivanšić [a,b,d,*]

[a] *Friedrich Schiller University Jena, Institute of Physical Chemistry, Helmholtzweg 4, Jena 07743, Germany*
[b] *Leibniz Institute of Photonic Technology, Research Department Functional Interfaces, Albert-Einstein-Str. 9, Jena 07745, Germany*
[c] *Institute of Inorganic Chemistry I, Ulm University, Albert-Einstein-Allee 11, Ulm 89081, Germany*
[d] *Friedrich Schiller University Jena, Center for Energy and Environmental Chemistry Jena (CEEC Jena), Lessingstraße 8, Jena 07743, Germany*

ARTICLE INFO

ABSTRACT

The synthesis and photophysical properties of the Ru-polypyridyl type complex $[(tbbpy)_2Ru(\mathbf{bptz})]^{2+}$ (**Ru-bptz**, tbbpy: 4,4'-*di-tert*-butyl-2,2'-bipyridine, **bptz**: 2,6-dipyrido-1,2,4,5-tetrazine), and the complexes $[(tbbpy)_2Ru(\mathbf{L})]^{2+}$ formed by inverse electron demand Diels Alder reaction (iEDDA) of **Ru-bptz** with with alkenes and alkynes, where **L** is 3,6-dipyrido-2,5-dihydropyridazine (**bpdhpn**) or 3,6-dipyrido-pyridazine (**bppn**) are described. A combination of steady-state and time-resolved spectroscopy complemented by the computation of state-specific absorption properties by means of time-dependent density functional theory reveals that the intense visible absorption band stems from Ru → tbbpy and Ru → **L** metal-to-ligand charge-transfer (MLCT) excitations. The studies show that lowest-lying **L**-centered MLCT states ($^3MLCT_L$) show comparably low emission quantum yields (3–9%) and lifetimes (90–150 ns). This correlates with the singlet oxygen generation ability, following the trend: **Ru-bppn** > **Ru-bpdhpn** > **Ru-bptz**.

Introduction

Photodynamic therapy has long been a viable alternative to surgery, radiation and chemotherapy in the treatment of cancer [1]. While there is a large variety of suitable photosensitizers available [2–4], ruthenium complexes have been especially promising [5,6] and have even reached clinical studies [7]. However, large breakthroughs have been rare, due to a lack of selectivity and remaining dark toxicity of the phototherapeutics. One approach to alleviate this issue is by either aiming for specific delivery through suitable cancer cell targeting concepts. There are two approaches available for targeted PDT therapeutics: Specific delivery through modification with suitable targeting moieties [4,8,9] or controllable activation by pre-treatment of the cancer cells with an activating agent [2].

Due to chemical complexity and variety of the targeting moieties, highly flexible conjugation techniques like click chemistry are employed. By relying on bioorthogonal click chemistry [10,11], the reaction can even take place in living cells. One method for bioorthogonal click chemistry is the so called inverse electron demand Diels Alder reaction (iEDDA) [12–14]. In this reaction, an electron poor diene, most commonly tetrazine, reacts with an electron rich alkene or alkyne with the elimination of nitrogen. While tetrazine based transition metal complexes have been under investigation for a long time [15], the application of these complexes in iEDDA conjugation is still in its infancy. Lo et al. demonstrated that such reactions are possible on tetrazines that are coordinated to a potentially luminescent iridium complexes [16–19]. Typically, the emission in such complexes is quenched, due to energy transfer between the photo-oxidized metal center and the tetrazine moiety [19]. Thus, alteration of the electronic structure of the tetrazine moiety *via* iEDDA reaction can be used to switch-on the metal complex emission. Additionally, through the same mechanism, the singlet oxygen photosensitization properties of the metal complexes can be controlled [19]. As it was shown that coordination increases the reaction speed of the iEDDA reaction [20,21], even

iridium triazine complexes have been shown to be usable conjugation agents [22].

A first non-luminescent ruthenium-cymene complex to be applicable for iEDDA conjugation has been shown by Ringenberg et al. [23]. As ruthenium-cymene complexes are not or non luminescent, no switching processes for the iridium complexes have been observed. 2,6-dipyrido-1,2,4,5-tetrazine has also been used as a bridging ligand for intra-molecular photocatalytic dyads [24].

In this study, we present the first biypyridine based ruthenium complex to undergo iEDDA conjugation, (tbbpy)$_2$Ru(**bptz**) (with 2,6-dipyrido-1,2,4,5-tetrazine (**bptz**)). Upon reaction with strained alkene (norbornene), successful generation of a complexed (full name here and then abbreviation) 3,6-dipyrido-2,5-dihydropyridazine (**bpdhpn**) occurs. The iEDDA with the strained alkyne, cyclooctyne, occurring within seconds leads to the aromatic (full name here and then abbreviation) 3,6-dipyrido-pyridazine (**bppn**) ligand. The dominant tautomeric form of the coordinated **bpdhpn** ligand could be identified by a combination of advanced optical spectroscopy and time dependent DFT analysis. All three complexes were investigated towards their ability to form singlet oxygen *via* sensitization. Here, the **bppn** complex showed promising properties, suggesting the possible usability as a controllable activation PDT agent. All complexes were extensively investigated regarding their photophysical properties by sophisticated time dependent spectroscopy methods.

Materials and methods

Steady-state absorption spectra were recorded on a Jasco V-670 spectrophotometer. For measuring the **steady-state emission** spectra a Jasco FP-8500 spectrofluorometer was used. The **emission lifetimes** were obtained by nanosecond time-resolved measurements. Therefore, a Continuum Surelite OPO Plus apparatus that is pumped by an Nd:YAG Laser was used as light source yielding pulses centered at 420 nm at a repetition rate of 10 Hz. The emission was recorded at 680 nm using a Hamamatsu R928 photomultiplier. **Emission quantum yields** were measured relatively to the quantum yield of [Ru(bpy)$_3$]$^{2+}$ (bpy = bipyridine, $\varphi_P = 9.5\%$ [25]) in aerated and de-aerated acetonitrile. **Steady-state NIR emission** spectra were obtained using a *Horiba Jobin-Yvon FluoroMax Plus-C* automated benchtop spectrofluorometer equipped with a 150 W Xe arc excitation lamp (horizontal, continuous wave), a R13456 photon-counting PMT detector (190−930 nm), a liquid-nitrogen (77 K) cooled InGaAs photodiode detector (800−1550 nm) and Czerny-Turner monochromators with 1200 groove/mm gratings blazed at 330 nm (excitation) and 500 nm (emission), or NIR gratings blazed at 1000 nm (emission) respectively. Emission spectra were corrected by multiplying with wavelength-specific factors given by the manufacturer to compensate for the detector response in the different spectral regions. Data were processed using the Origin-based software FluorEssence (v. 3.9.0.1 - hotfix #6.0, Origin 8.6001). Details on experimental parameters, sample preparations and data processing are given in the ESI.

The **ultrafast transient absorption** (TA) experiments were performed using a custom-built setup described in detail elsewhere [26,27]. The excited state dynamics was studied with white-light (generated by focusing a small portion of the amplifier output at 800 nm onto CaF$_2$) upon 400, 470, or 560 nm excitation. The fs-TA data was analysed using the KɪMoPᴀᴄᴋ tool [28]. Prior to global lifetime analysis, the data was arrival-time (chirp) corrected. The temporal resolution of the experiment is limited to 300 fs because of strong contributions of coherent artifact signals to the data interfere with reliable analysis of the pump-probe data at short delay times [29,30]. The pre-processed data was analysed using a sequential compartmental model, *i.e.*, treating the wavelength {λ_1, λ_2, ..., λ_n} and delay-time {Δt_1, Δt_2, ..., Δt_m} dependent profiles independently [31]. In the employed model, it is assumed that initially a single excited state is populated, which decays in an un-branched, unidirectional manner (A → B → ... → N), and can be described with the generalized rate equation: $\frac{dc_d}{dt} = -k_d \cdot c_d + k_{d-1} \cdot c_{d-1}$ (with dd $\in$ [N]). Thus, the concentration of each assumed species N (C$_{ad}$ with d $\in$ [N], a $\in$ [m]), is a linear combination of mono-exponential decays. Overall, the signals are described by $\Delta A_{ab} = \sum_{d=1}^{N} C_{ad} \cdot S_{db}$ (with a $\in$ [m], b $\in$ [n], d $\in$ [N]), where S$_{db}$ are the so-called species associated spectra (SAS) [32–34]. The optimized rate constants (k$_c$ with c $\in$ [N]) are associated with the spectral changes that occur upon the decay of the species $\sum_{d=c}^{N} S_{db}$ (with d $\in$ [N] and b $\in$ [n]). The errors of the fit parameters (k$_n$, n=1,2) are obtained in a confidence level of 95%.

Quantum chemical calculations for the Ru(II) complexes were performed using the Gaussian 16 program (revision B) [35]. First, the fully relaxed equilibrium geometries of **Ru-bptz, Ru-bpdhpn** - considering two tautomeric forms of the **bpdhpn** ligand, namely 3,6-dipyrido-2,5-dihydropyridazine (**bpdhpn1**) and 3,6-dipyrido-4,5-dihydropyridazine (**bpdhpn**) - and **Ru-bppn** were predicted in the singlet and triplet multiplicity. These simulations were performed at the density functional theory (DFT) level using the XC-B3LYP functional [36,37], with the def2SVP basis and their respective core potentials for all atoms [38,39]. To verify that the obtained geometries correspond to a minimum on the potential energy surface, a vibrational analysis was then performed. Second, the excited state properties (Franck-Condon region), *i.e.*, excitation energies and oscillator strengths, were calculated at the time-dependent DFT (TD-DFT) level of theory. Therefore, the 150 lowest excited states within the respective multiplicity of the ground state were calculated, *i.e.*, singlet-singlet and triplet-triplet transitions. The same functional, basis set, and nuclear potentials were used as in the ground state predictions. The effect of the interaction with the solvent acetonitrile ($\varepsilon = 35.688$, $n = 1.344$) on the properties of the ground and excited states was modelled by the variant of the electron density of the solute in the integral equation formalism of the polarizable continuum model [40,41]. The nonequilibrium solvation method was used to calculate the excitation energies. All calculations were performed using a D3 dispersion correction with Becke-Johnson damping [42].

Results and discussion

Synthesis and structural characterization

The complex **Ru-bptz**, bearing a 1,2,4,5-tetrazine ligand, was synthesized from the precursor [(tbbpy)$_2$RuCl$_2$] and 1,4-dihydro-3,6-dipyrido-1,2,4,5-tetrazine using standard complexation conditions [43]. After purification by size exclusion chromatography and crystallization from methanol/diethylether, the pure complex could be obtained as a violet solid. **Ru-bpdhpn** and **Ru-bppn** were formed *via* a click reaction of **Ru-bptz** and 2-norbornene in DCM over 24 h (see Fig. 1, top) or **Ru-bptz** and bicyclo[5.1.0]octan-8-ol (see Fig. 1, bottom) in methanol within a few seconds. Successful click reaction of the tetrazine ligand is visible by a color change from dark violet to red colors. MALDI-HR-MS and ESI-MS confirmed successful conversion to the product (see ESI section 1). The formation of the **Ru-bpdhpn** complex can lead to two tautomers in the ligand structures pictured in Fig. 1.

Ground state absorption properties

To study the influence of the ligand structure on the electronic transitions in the Franck Condon region, steady-state ground state absorption spectroscopy was applied. The assignment of the electronic transitions and their electronic nature is based on TD-DFT calculations. The absorption spectra of **Ru-bptz, Ru-bpdhpn**, and **Ru-bppn** in acetonitrile (see Fig. 2 and Table 1) are composed of two major regions namely, an intense $\pi\pi^*$ absorption band at around 300 nm (4.0 – 6.5 × 10^4 M^{-1}cm^{-1}) and a weaker, broad, and structured metal-to-ligand charge-transfer (MLCT) absorption band in the visible range between 350 and 600 nm (0.5–1.5 × 10^4 M^{-1}cm^{-1}). The absorption spectra of the three complexes essentially differ in the structure and position of the
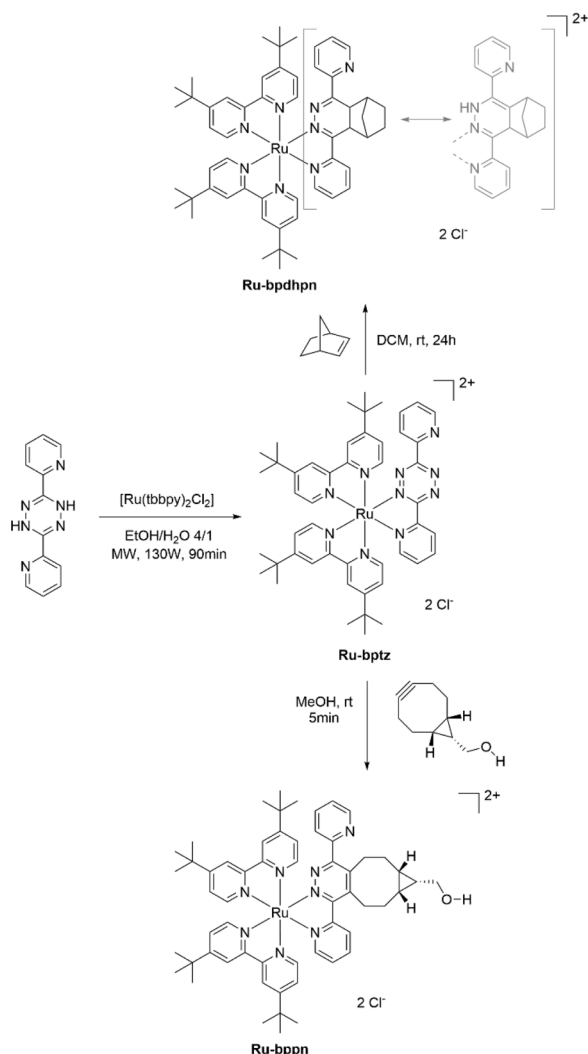
Fig. 1. Synthetic access of the tetrazine complex **Ru-bptz** and further functionalization via iEDDA click reaction with 2-norbornene (alkene) or bicyclo [5.1.0]octan-8-ol (alkyne) yielding **Ru-bpdhpn** (with its tautomeric ligand in grey) or **Ru-bppn**, respectively.

MLCT bands. The underlying MLCT transitions can be divided into three categories based on the involved π*-acceptor orbitals, which are located on the tbbpy ligands (MLCT$_{bpy}$), localized on the tetrazin (tz) or pyridazine (pn) moiety (MLCT$_{tz/pn}$) of **bptz** and **bppn**, and delocalized on the **bptz, bpdhpn**, or **bppn** ligand (MLCT$_{bp}$, see charge density

differences (CDDs) in Fig. 2).

The MLCT absorption band of **Ru-bptz** reveals two major features centered at 400 and 520 nm, associated with MLCT transitions. Since the **bptz** is an electron-deficient ligand, the electron density at the central Ru(II) ion is decreased with respect to the homoleptic reference complex [Ru(tbbpy)$_3$]$^{2+}$. Consequently, the MLCT$_{bpy}$ transitions (*circa* 396 nm, see Fig. S15) are blue shifted (by 0.33 eV) compared to [Ru(tbbpy)$_3$]$^{2+}$ (442 nm). On the other hand, the **bptz**-centered π*-orbitals are comparably low-lying with respect to π*$_{bpy}$ orbitals due to the electron-deficiency [15]. Thus, the absorption features at 529 nm (2.34 eV) and 461 nm (2.69 eV, see Table 1 and Fig. S15), are assigned to MLCT$_{bptz}$ (S$_6$) and MLCT$_{tz}$ (S$_7$) transitions, respectively [44], which is supported by TD-DFT (see CDDs in Fig. 2 and Table S4).

In contrast to the **bptz** ligand, **bpdhpn** and **bppn** are moderately strong π-electron donors (electron-rich ligands) comparable to the tbbpy ligand. Therefore, the MLCT$_{bpy}$ states are close in energy to those of [Ru (tbbpy)$_3$]$^{2+}$, which is supported by TD-DFT. Experimentally, this is reflected in the similar maximum of the MLCT$_{bpy}$ absorption band, which is at around 442 nm for **Ru-bpdhpn** (S$_3$), **Ru-bppn** (S$_8$), and 458 nm for [Ru(tbbpy)$_3$]$^{2+}$ [45]. In addition to the MLCT$_{bpy}$ features, the absorption spectra of **Ru-bpdhpn** and **Ru-bppn** show absorption features centered at 530 nm (2.34 eV) and 462 nm (2.68 eV), respectively (*cf.* Fig. S15). Consistent with **Ru-bptz**, these low-lying absorption features are associated with Ru → **bpdhpn** (S$_{3,10}$) and Ru → **bppn** MLCT transitions (S$_{5,9}$), respectively [46]. TD-DFT supports, that the **bppn**-centered π* acceptor orbitals are higher in energy compared to those of **bpdhpn** (see Tables S6 and S7). Noteworthy, the absorption spectrum of **Ru-bpdhpn** shows additional features at around 360 nm, which can be attributed to ππ* transitions on the **bpdhpn** ligand (S$_{12}$, *cf.* Fig. 2).

Since ligand **bpdhpn** can tautomerize, the ground state equilibrium structure of **Ru-bpdhpn** was explored by means of DFT. Therefore, the two tautomeric forms of **bpdhpn**, namely 3,6-dipyrido-2,5-dihydropyridazine (**bpdhpn1**) and 3,6-dipyrido-4,5-dihydropyridazine (**bpdhpn**) were considered. To this end, the **bpdhpn** tautomer turned out as most stable isomer (by 0.17 eV). TD-DFT indicates that only **Ru-bpdhpn** absorbs via both a MLCT$_{bpy}$ (S$_8$) and a lower-lying MLCT$_{bpdhpn}$ (S$_3$, *cf.* Fig. 3 and Table S6), while the absorption of **Ru-bpdhpn1** is due to MLCT$_{bpy}$ transitions only (S$_{5-8}$, see Table S5). Thus, we associate the experimentally observed spectra with the **Ru-bpdhpn** tautomer.

(Spectro-)Electrochemistry

The reduction potentials of the complexes were determined by cyclic voltammetry (CV, see Table 1 and Fig. S13) to **Ru-bptz**: -1.0 V *vs.* Fc$^{0/+}$; **Ru-bpdhpn**: -1.6 V *vs.* Fc$^{0/+}$; **Ru-bppn**: -2.0 V *vs.* Fc$^{0/+}$. The CV of **Ru-bptz** shows a reversible reduction at -0.78 V assigned to the tetrazine moiety [48–51]. Further reduction events occur at -1.68, -2.02 and -2.22 V. We associate the reduction at -1.68 V to the tetrazine ligand and the
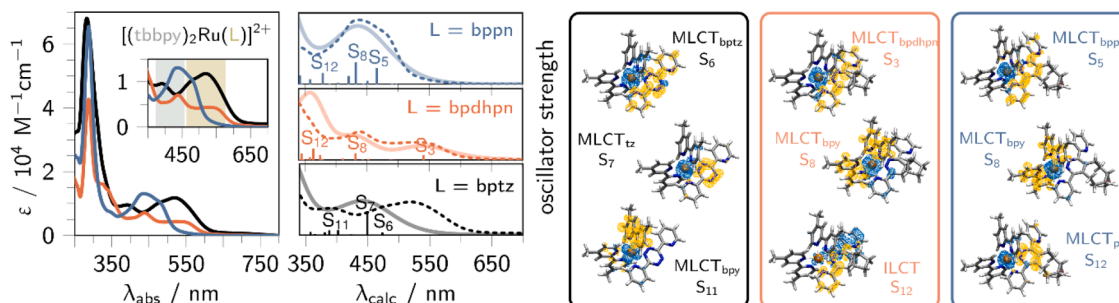

Fig. 2. Experimental (left) and simulated (middle) UV/vis absorption spectra of **Ru-bptz** (black), **Ru-bpdhpn** (orange) and **Ru-bppn** (blue) in acetonitrile and some selected charge-density differences (right). Excitation occurs from blue to yellow (ρ = ±0.0015). The inset in the experimental UV/vis absorption plot shows the MLCT absorption band, where the regions of tbbpy and **bptz, bpdhpn** or **bppn** (L) located MLCT transitions are highlighted in grey and yellow, respectively. The simulated vertical excitation energies and corresponding oscillator strengths are depicted as bars, which were spectrally broadened using Gaussian functions with a full width at half height of 0.3 eV.

Table 1

Summary of the photophysical properties of Ru-bptz, Ru-bpdhpn, Ru-bppn and [Ru(tbbpy)$_3$]$^{2+}$ (Ru-tbbpy) [47] in acetonitrile: absorption and emission maxima (λ_{abs}^m and λ_P^m), half-wave reduction potentials (obtained by cyclic voltammetry in acetonitrile (1 mM) in the presence of 0.1 M n-Bu$_4$NPF$_6$, see Figure S13; top row: non-tbbpy ligands; bottom row: tbbpy ligands), emission lifetimes (τ_P), emission quantum yields (φ_P) in aerated and deaerated acetonitrile (values in braces), as well as radiative ($\tau_r = \varphi_P^{-1} \cdot \tau_P$) and non-radiative excited state lifetimes ($\tau_{nr} = (1 - \varphi_P)^{-1} \cdot \tau_P$) obtained according to the energy gap law.

complex	λ_{abs}^m (ε_{abs}^m) / nm (10^4 M^{-1}cm^{-1})	λ_P^m (T$_1$-S$_0$)/ nm (eV)	E$_{red}^{1/2}$/ V (vs. Fc$^{0/+}$)	τ_P/ ns	φ_P/ %	τ_r (τ_{nr}) / μs (ns)
Ru-bptz	529 (1.16), 461 (0.91)	700 (1.77)	-0.78, -1.68 -2.05, -2.22	88	0.0 (3.5)	2.5 (91)
Ru-bpdhpn	530 (0.44), 442 (0.70)	680 (1.83)	-1.30, -1.84, -2.45 -2.07, -2.22	129	0.2 (4.1)	3.1 (135)
Ru-bppn	475 (1.08), 430 (1.3)	675 (1.82)	-1.67, -2.49 -2.01, -2.26	150	0.5 (9.1)	1.7 (165)
Ru-tbbpy	467 (1.67)	606 (2.05)	-1.80, -2.01, -2.28	860	(9.5)	9.1 (950)
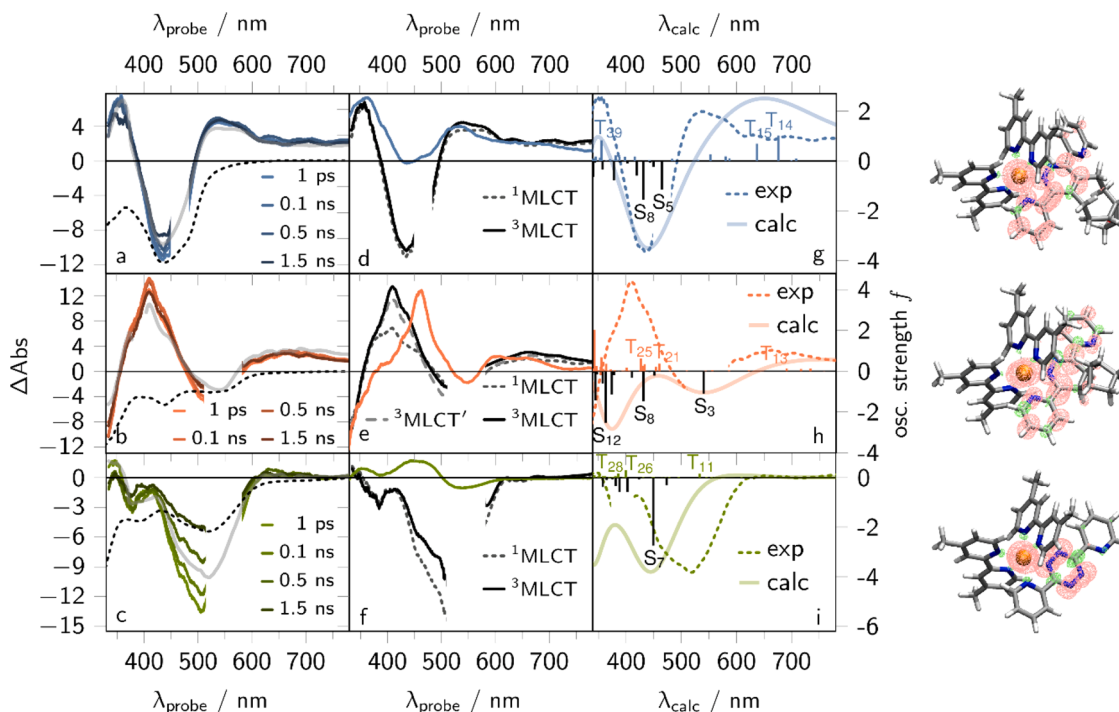
Fig. 3. Ultrafast transient absorption (TA, **a–c**) and species associated spectra (SAS, **d–f**) of **Ru-bppn** (**a** and **d**), **Ru-bpdhpn** (**b** and **e**), and **Ru-bptz** (**c** and **f**) upon 480 nm (**Ru-bppn**, 0.5 mW) or 560 nm excitation (**Ru-bpdhpn** and **Ru-bptz**, 0.2 mW) in acetonitrile (sample concentration of *circa* 0.2 mM). For each complex a scaled TA spectrum collected upon 400 nm excitation (0.5 mW) in acetonitrile at a delay time of 1 ps is shown in grey (grey, solid lines in **a – c**, see also Fig. S19). The black, dashed lines in the TA spectra show the scaled and inverted ground state absorption spectra of the respective complexes. The difference spectra obtained from spectro-electrochemistry, *i.e.*, **Ru-L**$^{\bullet-}$–**Ru-L** (**L = bptz, bpdhpn**, or **bppn**) are shown in the insets **d – f** as colored lines. Simulated difference spectra (solid lines in the subplots **g – i**) for a S$_0$ to T$_1$ excitation of **Ru-bppn** (blue, **g**), **Ru-bpdhpn** (orange, **h**), and **Ru-bptz** (green, **i**) in acetonitrile. The respective spin density distributions of the optimized T$_1$ (^{3}MLCT) states are shown on the right panel. The TD-DFT simulated vertical transition energies and corresponding oscillator strengths are represented as bars (S$_0$: negative, T$_1$: positive), which were spectrally broadened using Gaussian functions (full-width half-height of 0.3 eV). For reasons of comparability, the 1.5 ns TA spectrum of the respective complex is shown as dashed line.

others to the tbbpy ligands. Like in comparable cymene complexes [20], the first reduction wave occurs at -1.3 V for **Ru-bpdhpn**. The reduction wave is followed by reversible waves at -1.84, -2.07 and -2.22 V. Similar to the parent complex, these can be associated with the pyrazine and tbbpy ligands [52]. A fourth reduction wave occurs at -2.45 V. **Ru-bppn** shows a reversible reduction wave at -1.67 V linked to the one– electron reduction of the pyrazine ligand [53]. Additionally, further reduction waves occur at -2.01 V, -2.26 V (both tbbpy) and -2.49 V. Oxidation of the ruthenium center is overlayed by the chloride reduction and occurs at around 0.8 V for **Ru-bpdhpn** and **Ru-bppn**.

After the determination of the reduction and oxidation potentials, the UV/vis absorption spectra of **Ru-bptz, Ru-bpdhpn**, and **Ru-bppn** were recorded upon single-electron reduction (see coloured lines in Fig. 3**d**, **e**, and **f** as well as Fig. S16). The spectroelectrochemical studies confirm that the first, single-electron reduction of **Ru-bptz, Ru-bpdhp**,

and **Ru-bppn** occurs on the **bptz, bpdhpn**, or **bppn** ligand, respectively. This is reflected in the decrease of the MLCT$_L$ (L = **bptz, bpdhpn**, or **bppn**) and **bpdhpn**-centered $\pi\pi^*$ features at around 360 nm upon single-electron reduction. Moreover, the MLCT absorption between 400 and 500 nm rises. The spectra of the reduced complexes, namely **Ru-bptz**$^{\bullet-}$, **Ru-bpdhpn**$^{\bullet-}$, and **Ru-bppn**$^{\bullet-}$ resemble the absorption spectrum of [Ru (tbbpy)$_3$]$^{2+}$ (*cf.* green line in Fig. S16, right). Thus, the new arising absorption features at *circa* 440 nm stem from MLCT$_{bpy}$ transitions. Hence, the data supports the character of the low-lying absorption features, *i.e.*, MLCT states with excess electron density on the **bptz, bppn** or **bpdhpn** ligand, respectively.

Emission properties

Steady state and time-resolved emission studies were performed. The

emission of **Ru-bptz** in acetonitrile is centered at 700 nm (1.77 eV). In contrast, the emission of **Ru-bpdhpn** and **Ru-bppn** is blue-shifted to 680 nm (1.82 eV) and 675 nm (1.83), respectively. This is consistent with previous reports on structurally related Ru(II) complexes bearing pyrazine ligands [46,54]. For all three complexes the emission maximum is red-shifted compared to the homoleptic reference complex $[Ru(tbbpy)_3]^{2+}$, indicating that the emission stems from the ^{3}MLCT states with excess electron density on the **bptz, bpdhpn**, or **bppn** ligand, respectively [46,54]. TD-DFT also predicts that the T_1 states show excess electron density on the respective ligands. The emission lifetimes and quantum yields follow the trend **Ru-bptz** (88 ns, 3.5%) < **Ru-bpdhpn** (129 ns, 4.1%) < **Ru-bppn** (150 ns, 9.1%). This trend can be explained by the energy gap law (see Fig. S18) with an increasing T_1-S_0 energy gap in the order **Ru-bppn** > **Ru-bpdhpn** > **Ru-bptz** [55–57]. Similar observations are reported by Lo et al., showing that the non-emissive tetrazine-containing iridium complexes experience significant emission enhancement upon iEDDA reaction with alkenes or alkynes forming a pyridazine or dihydropyridazine derivative. In line with our results, the emission lifetime and intensity of the pyridazine derivative (here: **Ru-bppn**) is higher than that of the dihydropyridazine derivative[16,19,58].

Photoinduced Dynamics

To study the photoinduced processes that yield the population of the long-lived excited ^{3}MLCT states, transient absorption (TA) spectroscopy was employed. The discussion starts with the excited state properties of **Ru-bptz** and **Ru-bpdhpn** upon excitation at 560 nm, and **Ru-bppn** upon 480 nm excitation in acetonitrile (*cf.* Fig. 3**a–c** and **S18**), *i.e.*, in resonance with the MLCT$_{bptz}$, MLCT$_{bpdhpn}$ and MLCT$_{bppn}$ transitions, respectively. The results are compared to the TA spectra collected upon 400 nm excitation (*cf.* grey curve in Figs. 3**a–c** and **S19**), *i.e.*, upon additional excitation of MLCT$_{bpy}$ states. In addition, the influence of the polarity of the solvent (acetonitrile: $\varepsilon = 37.5$; dichloromethane: $\varepsilon = 8.9$) on the ultrafast processes is investigated (*cf.* Figs. **S19** and **S20**).

Photoinduced dynamics in acetonitrile. Ru-bptz

The fs-TA spectra of **Ru-bptz** in acetonitrile upon 400 and 560 nm excitation show instantaneous ground state bleach (GSB) between 360 and 600 nm and comparably weak excited state absorption (ESA) between 600 and 700 nm and centered at 345 nm. Within the first 100 ps, the ESA at 345 nm decreases while the signals between 360 and 600 nm increase. Global analysis of the TA data using a sequential kinetic scheme reveals two characteristic time-constants, namely $\tau_1 = (140 \pm 70)$ ps and $\tau_2 = (2.1 \pm 0.1)$ ns.

The spectral changes associated with τ_1, describe the decrease of ESA centered at 355 nm and partial GSB recovery (450–600 nm). The maximum at 355 nm can be associated with $\pi\pi^*$ transitions on the formally reduced **tbbpy** [59] and **bptz** ligands. The latter is revealed from spectro-electrochemistry results, that indicate an increase of absorption at around 350 nm upon single-electron reduction on the **bptz** ligand of **Ru-bptz** (*cf.* green line in Figs. 3**f** and **S16**). Since, the ratio between the ESA at 355 nm and the GSB at 500 nm increases upon shifting the excitation wavelength from 550 to 400 nm (*cf.* grey *vs.* light-green light in Fig. 3**c**), we associate τ_1 with vibrational cooling, solvent reorganization, and inter-ligand hopping from the **tbbpy** to the **bptz** manifold [60–63]. Thereby, an MLCT state with excess electron density localized on the tetrazine moiety of the **bptz** ligand (^{3}MLCT$_{tz}$) is formed. The fact that the TA-spectrum associated with that ^{3}MLCT$_{tz}$ state primarily shows GSB features, is supported by TD-DFT, revealing that the LMCT and **bptz**-centered $\pi\pi^*$ excited state absorption features are weak (*e.g.*, T_{26}, 399 nm, $f = 0.030$) compared to the ground state absorption features (*e.g.*, S_7, 449 nm, $f = 0.274$, see Fig. 3**i** as well as **Tables S3** and $S7$). Moreover, TD-DFT predicts an ESA feature at 533 nm (T_{11}, see Fig. 3**i** and **Table S8**), which is in agreement with previous

reports about the absorption features of the ^{3}**bptz** ligand [64,65]. The characteristic time-constant τ_2 reflects partial GSB recovery between 350 and 600 nm, *i.e.*, a decrease of the respective TA signals over 2 ns by *circa* 50%.

Taking into account the phosphorescence lifetime ($\tau_P = 88$ ns) and the emission quantum yield ($\varphi_P = 3.5\%$), a radiative ($\tau_r = \varphi_P^{-1} \cdot \tau_P$) and non-radiative lifetime ($\tau_{nr} = (1-\varphi_P)^{-1} \cdot \tau_P$) of the long-lived ^{3}MLCT$_{tz}$ excited state can be calculated to be 2.5 µs (τ_r) and 91 ns (τ_{nr}), respectively (see **Table 1**). The process associated with τ_{nr} only accounts for a 3%-signal decrease within the range of accessible delay times (maximum accessible delay time: 2 ns), we associate τ_2 with the non-radiative decay of a subset of ^{3}MLCT$_{tz}$ states via (thermally) accessible metal-centered (^{3}MC) states [66,67]. In dichloromethane, the same process is observed at a similar rate (see Fig. S21a). We assume that the **bptz** ligand exists in different conformers in the ^{3}MLCT$_{tz}$ excited state manifold. Based on the DFT results for the T_1 state, we assume that the **bptz** ligand is planar in the long-lived state (see structure of T_1 state in Fig. 3). The decreased ^{3}MC excited state lifetime with respect to [Ru (tbbpy)$_3$]$^{2+}$ [67] can be attributed to the stabilization of the respective states in **Ru-bptz** due to the decreased electron density at the Ru-center. This further supports the comparably low emission quantum yield (3.5% *vs.* 9.5%, *cf.* **Table 1**).

Ru-bpdhpn

The initial TA spectrum ($\Delta t = 0.3$ ps) of **Ru-bpdhpn** collected upon excitation at 400 and 560 nm excitation (see Figs. 3**b, S20c**, and **S21c**), *i.e.*, in resonance with the MLCT$_{bpy}$ and MLCT$_{bpdhpn}$ transitions, shows GSB centered at 530 nm and 340 nm, which resemble the shape of the **bpdhpn**-centered MLCT and $\pi\pi^*$ ground state absorption band. The GSB features are accompanied by comparably strong ESA centered at around 400 nm and weaker, unstructured ESA features between 600 and 750 nm. By direct comparison to the difference spectrum of **Ru-bpdhpn**$^{\bullet-}$ and **Ru-bpdhpn** (see orange line in Fig. 3**e**), the ESA features can be associated with $\pi\pi^*$ and LMCT transitions that stem from the excess electron density on the **bpdhpn** ligand. This can be further supported by TD-DFT, showing that the optimized T_1 state exhibits $\pi\pi^*$ (T_{25}, 402 nm) and LMCT absorption features (T_{13}, 484 nm, see **Table S10**). In the first 100 ps, the ESA at 400 nm increases. Within the time-range of the measurement (2 ns), all signals partially decay (8%).

The spectral changes can be quantitatively described by three characteristic time constants, namely $\tau_1 = (0.2 \pm 0.1)$ ps, $\tau_2 = (121 \pm 66)$ ps, and $\tau_3 = (4.2 \pm 1.1)$ ns (see Figs. 3, **S18** and **S19**). The spectral changes associated with τ_1 describe the build-up of ESA at between 600 and 750 nm as well as ranging from 350 to 460 nm. The latter ESA band shows pronounced features, *i.e.*, a maximum at 405 nm and shoulders at 450 and 360 nm. We associate this with $\pi\pi^*$ transitions of the formally reduced **tbbpy** (350 nm [60,67]) and **bpdhpn** ligand spheres (400−450 nm, see orange line in Fig. 3**e**). Hence, τ_1 can be attributed to vibrational cooling [60–63] populating ^{3}MLCT$_{tbbpy}$ and ^{3}MLCT$_{bpdhpn}$ states. The process associated with τ_2 increases the ESA at 400 and 450 nm at the expanse of the features at 360 nm (see SAS(τ_2) in Fig. 3**e**). We associate this with inter-ligand hopping from the **tbbpy** to the **bpdhpn** manifold. Finally, the spectral changes associated with τ_3 comprise a minor, 8%-decay of the overall TA signal (see solid, black line in Fig. 3**e**). As the non-radiative decay (see **Table 1**) of the excited state in the 2 ns measurement window implies a signal depletion of about 2%, we assign τ_3 to the non-radiative decay of a subset of ^{3}MLCT$_{bpdhpn}$ states (conformational isomers) *via* the ^{3}MC manifold, forming the long-lived ^{3}MLCT$_{bpdhpn}$ states. That this deactivation process is faster than for **Ru-bptz** ($\tau_2 \approx 2$ ns) indicates a smaller energy gap between the long-lived, emissive ^{3}MLCT and the non-emissive ^{3}MC states in case of **Ru-bpdhpn**, which can be attributed to the **bpdhpn** being more electron-rich than the **bptz** ligand.

Ru-bppn

The 0.3 ps TA spectrum of **Ru-bppn** collected upon 400 and 470 nm excitation (see Figs. 3**a**, **S20b**, and **S21b**) shows a shape typically observed for Ruthenium tris-bipyridine-type complexes: A strong GSB between 400 and 500 nm is accompanied by ESA centered at 360 and 520 nm [60,67]. However, the ratio between the ESA and GSB features of **Ru-bppn** is higher than for $[Ru(tbbpy)_3]^{2+}$ [67]. This can be attributed to $\pi\pi^*$ and LMCT features in the formally reduced **bppn** moiety, which is supported by TD-DFT (see **Table S11**). Within the experimentally accessible delay-time window of 2 ns, the TA signals, *i.e.*, the ESA at 360 nm and the GSB features decrease by *circa* 20%. Global lifetime analysis reveals two characteristic time-constants, namely $\tau_1 = (280 \pm 80)$ ps, $\tau_2 = (7.5 \pm 2.0)$ ns. The spectral changes associated with τ_1 describe the build-up of ESA between 500 and 600 nm. According to the spectroelectrochemical measurements, this ESA can be attributed to a state, in which the **bppn** ligand is reduced, *i.e.*, a $^3MLCT_{bppn}$ state. This is supported by TD-DFT predicting, that such a $^3MLCT_{bppn}$ state shows LMCT features between 500 and 700 nm (*e.g.*, T_{14-18}) and $\pi\pi^*$ absorption at around 350 nm (T_{39}, see Figs. 3**g** and **S25**, and **Table S11**). Thus, we associate τ_1 with vibrational cooling and inter-ligand hopping [60–63], populating the lowest-lying ^3MLCT state, characterized by excess electron density in the **bppn** ligand sphere. In turn, the TA signals partially decay with τ_2 (7.5 ns), which we associate – in analogy to **Ru-bptz** and **Ru-bpdhpn** – with the non-radiative decay of specific conformational isomers of $^3MLCT_{bppn}$ states through the thermally accessible ^3MC states.

Lifetime of excited-states

The lifetimes for the non-radiative decay of a subset of $^3MLCT_L$ (**L** = **bptz, bpdhpn, bppn**) states *via* the ^3MC manifold follow the same order as the emission lifetimes and quantum yields, *i.e.*, **Ru-bptz** (≈ 2 ns) < **Ru-bpdhpn** (≈ 4 ns) < **Ru-bppn** (≈ 8 ns). Furthermore, the electron density at the central Ru-ion follows the same trend, indicating that the ^3MC states of **Ru-bptz** are more accessible (stabilized) with respect to **Ru-bppn**, causing a rapid decay of the TA signals [68,69]. This underlines that the emission efficiency is primarily governed by the relative energy of the $^3MLCT_L$ (**L** = **bptz, bpdhpn**, or **bppn**) and ^3MC states, *i.e.*, the electronic character of the ligand **L** and the central Ru-ion.

Singlet-oxygen generation

The potency of the complexes towards singlet oxygen generation was evaluated by recording the absorbance of mixtures of **Ru-bptz, Ru-bpdhpn**, or **Ru-bppn** (5 µM) and 9,10-anthracenediyl-bi(methylene)-dimalonic acid (ABDA, 25 µM) [70,71] under photoexcitation at 470 nm (LED, 54 mW·cm⁻², see Figs. 4 and **S20**). For reasons of comparability, a mixture of $[Ru(bpy)_3]^{2+}$ (bpy = bipyridine) and ABDA was used as a benchmark system. Fig. 4 shows the absorption changes of ABDA at 380 nm over 30 min LED irradiation at 470 nm (54 mW·cm⁻²) for **Ru-bptz, Ru-bpdhpn, Ru-bppn** and $[Ru(bpy)_3]^{2+}$. While all complexes produce significantly less singlet oxygen than $[Ru(bpy)_3]^{2+}$, there are noticeable differences between the tetrazine and pyridazine complexes: Both, **Ru-bptz** and **Ru-bpdhpn** show barely any $^1O_2$ production within the 30 min of LED-illumination. This is reflected in the decrease of the ABDA absorption at 380 nm by a factor of 1.08. However, this factor is 1.28 in case of **Ru-bppn**, indicating a striking increase in $^1O_2$ production with respect to **Ru-bptz** and **Ru-bpdhpn**. This can be explained by the following two properties: (*i*) the reduction potential of the photoexcited **Ru-bppn** is the lowest (E(**Ru-bppn**•⁺/*Ru-bppn**) = 0.15 V) and (*ii*) the emission lifetime and quantum yield of **Ru-bppn** is the highest in the series of the three complexes studied (see Tables 1 and **S1**). This agrees with previous findings revealing that the emission of Ir(III) complexes bearing a tetrazine or dihydropyridazine extended ligand is quenched due to the population of tetrazine/dihydropyridazine centered MLCT
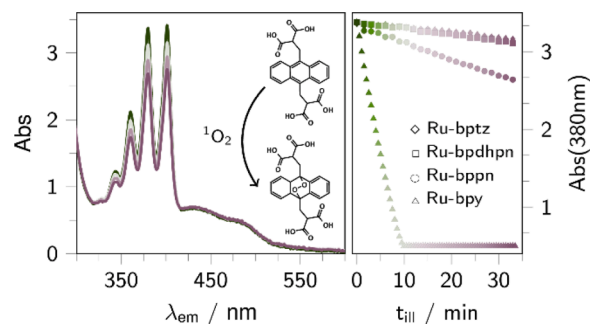
Fig. 4. Left: Normalized absorption spectrum of a mixture of **Ru-bppn** (5 µM) and ABDA (25 µM) in PBS-buffered aqueous solution (pH 7.4) and upon LED-illumination at 470 nm (45 mW cm⁻²) for 10, 20 and 30 min, showing a decrease of the structure ABDA absorption features between 350 and 410 nm. Right: Monitoring of the absorption changes at 380 nm for mixtures of **Ru-bptz** (◇), **Ru-bpdhpn** (□), **Ru-bppn** (○), or **Ru-bpy** (△, each 5 µM) with ABDA (25 µM) in PBS-buffered aqueous solution (pH 7.4, see also Fig. S22).

and LLCT states *via* electron and energy transfer. Contrary, ligand extension by a pyridazine unit causes no further emission quenching [19].

All three complexes show no changes in their absorption behavior (see Fig. S22) during the experiment, suggesting that, especially for **Ru-bpdhpn**, no singlet oxygen driven oxidation occurs. Consumption of singlet oxygen by the ligand itself would have a suitable explanation for its low generation efficiency. This is in contrast to our recent findings showing that a dihydropyridazine bridge of a bimetallic photocatalyst can be dehydrogenated with singlet oxygen [24]. Furthermore, this is contrary to the results of Ringenberg et al. who showed that dihydropyridazine is oxidized by oxygen in the presence of a catalyst [23]. To validate the ability of the complexes to sensitize singlet oxygen, its NIR phosphorescence at 1270 nm was monitored upon excitation of samples of constant optical density in air-equilibrated acetonitrile and deuterated methanol, solvents for which singlet oxygen quantum yields of the used benchmark **Ru-bpy** are literature-known [72,73]. However, under the experimental parameters, **Ru-bptz** decomposed rapidly in methanol and slight spectral changes were observed for **Ru-bpdhpn**, allowing no quantification. Nevertheless, the same trend in singlet oxygen phosphorescence peak areas could be observed, proving the potential of **Ru-bppn** as model compound for therapeutically active agents. (Figs. S23, 24 and Table S3).

Conclusion

In conclusion, we show the successful iEDDA reaction of a tetrazine ligand coordinated to a Ru-ion (**Ru-bptz**) with the strained alkene 2-norbornene (slow) or the alkyne (1R,8S,9S)-bicyclo[6.1.0]non-4-yne-9-yl-methanol (fast) forming the respective Ru complexes with a dihydropyridazine (**Ru-bpdhpn**) or pyridazine ligand (**Ru-bppn**). The three complexes show strong visible absorption, to which both tbbpy and **L**-centered MLCT states (**L** = **bptz, bppn**, and **bpdhpn**) contribute. Spectro-electrochemical and ultrafast transient absorption studies complemented by TD-DFT predict state-specific absorption properties and reveal that photoexcitation between 400 and 550 nm leads to the formation of an emissive ^3MLCT state with excess electron density on the **L**-ligand. It was found that the photophysical properties, such as emission lifetime (90–150 ns) and quantum yield (3–9%) as well as singlet-oxygen generation, are tuned by the alteration of the electronic properties of the tetrazine-based ligands. The generated singlet oxygen was not found to oxidize **Ru-bpdhpn**. The increase in singlet oxygen production (**Ru-bppn** > **Ru-bpdhpn** ≈ **Ru-bptz**) suggests, that a suitable alkyne functionalization to target certain cells could be used to switch on singlet oxygen production only in cells where the alkyne is present.

Among the three studied coordination compounds, **Ru-bppn**

emerges as the complex with the longest excited state lifetime (150 ns), highest emission quantum yield ($\approx$9%), and highest singlet-oxygen generation. Beyond rationalizing existing literature of structurally related molecules, we show that improved metal-ligand interactions give rise to that increase of emission quantum yield and lifetime due to destabilization of non-emissive ^{3}MC states with respect to the emissive ^{3}MLCT$_{bppn}$ states.

Declaration of Competing Interest

The authors declare that they have no known competing financial interests or personal relationships that could have appeared to influence the work reported in this paper.

Acknowledgments

Supplementary materials

Supplementary material associated with this article can be found, in the online version, at doi:10.1016/j.jpap.2022.100130.

Literature

[1] D.E.J.G.J. Dolmans, D. Fukumura, R.K. Jain, Photodynamic therapy for cancer, Nat. Rev. Cancer. 3 (2003) 380–387, https://doi.org/10.1038/nrc1071.

[2] A. Turksoy, D. Yildiz, E.U. Akkaya, Photosensitization and controlled photosensitization with BODIPY dyes, Coord. Chem. Rev. 379 (2019) 47–64, https://doi.org/10.1016/j.ccr.2017.09.029.

[3] M. Ethirajan, Y. Chen, P. Joshi, R.K. Pandey, The role of porphyrin chemistry in tumor imaging and photodynamic therapy, Chem. Soc. Rev. 40 (2011) 340–362, https://doi.org/10.1039/B915149B.

[4] J.C.S. Simões, S. Sarpaki, P. Papadimitroulas, B. Therrien, G. Loudos, Conjugated photosensitizers for imaging and PDT in cancer research, J. Med. Chem. 63 (2020) 14119–14150, https://doi.org/10.1021/acs.jmedchem.0c00047.

[5] C. Reichardt, S. Monro, F.H. Sobotta, K.L. Colón, T. Sainuddin, M. Stephenson, E. Sampson, J. Roque, H. Yin, J.C. Brendel, C.G. Cameron, S. McFarland, B. Dietzek, Predictive strength of photophysical measurements for in vitro photobiological activity in a series of Ru(II) polypyridyl complexes derived from π-extended ligands, Inorg. Chem. 58 (2019) 3156–3166, https://doi.org/10.1021/acs.inorgchem.8b03223.

[6] G. Shi, S. Monro, R. Hennigar, J. Colpitts, J. Fong, K. Kasimova, H. Yin, R. DeCoste, C. Spencer, L. Chamberlain, A. Mandel, L. Lilge, S.A. McFarland, Ru(II) dyads derived from α-oligothiophenes: a new class of potent and versatile photosensitizers for PDT, Coord. Chem. Rev. 282–283 (2015) 127–138, https://doi.org/10.1016/j.ccr.2014.04.012.

[7] S. Chamberlain, H.D. Cole, J. Roque, D. Bellnier, S.A. McFarland, G. Shafirstein, TLD1433-mediated photodynamic therapy with an optical surface applicator in the treatment of lung cancer cells in vitro, Pharmaceuticals 13 (2020) 137, https://doi.org/10.3390/ph13070137.

[8] T. Wang, N. Zabarska, Y. Wu, M. Lamla, S. Fischer, K. Monczak, D.Y.W. Ng, S. Rau, T. Weil, Receptor selective ruthenium-somatostatin photosensitizer for cancer targeted photodynamic applications, Chem. Commun. 51 (2015) 12552–12555, https://doi.org/10.1039/C5CC03473F.

[9] N.M. Vegi, S. Chakrabortty, M.M. Zegota, S.L. Kuan, A. Stumper, V.P.S. Rawat, S. Sieste, C. Buske, S. Rau, T. Weil, M. Feuring-Buske, Somatostatin receptor mediated targeting of acute myeloid leukemia by photodynamic metal complexes for light induced apoptosis, Sci. Rep. 10 (2020) 371, https://doi.org/10.1038/s41598-019-57172-6.

[10] C.R. Bertozzi, A decade of bioorthogonal chemistry, Acc. Chem. Res. 44 (2011) 651–653, https://doi.org/10.1021/ar200193f.

[11] N.K. Devaraj, The future of bioorthogonal chemistry, ACS Cent. Sci. 4 (2018) 952–959, https://doi.org/10.1021/acscentsci.8b00251.

[12] M.L. Blackman, M. Royzen, J.M. Fox, Tetrazine ligation: fast bioconjugation based on inverse-electron-demand Diels−Alder reactivity, J. Am. Chem. Soc. 130 (2008) 13518–13519, https://doi.org/10.1021/ja8053805.

[13] B.L. Oliveira, Z. Guo, G.J.L. Bernardes, Inverse electron demand Diels–Alder reactions in chemical biology, Chem. Soc. Rev. 46 (2017) 4895–4950, https://doi.org/10.1039/C7CS00184C.

[14] A.-C. Knall, C. Slugovc, Inverse electron demand Diels–Alder (iEDDA)-initiated conjugation: a (high) potential click chemistry scheme, Chem. Soc. Rev. 42 (2013) 5131, https://doi.org/10.1039/c3cs60049a.

[15] W. Kaim, The coordination chemistry of 1,2,4,5-tetrazines, Coord. Chem. Rev. 230 (2002) 127–139, https://doi.org/10.1016/S0010-8545(02)00044-9.

[16] S.P.-Y. Li, A.M.-H. Yip, H.-W. Liu, K.K.-W. Lo, Installing an additional emission quenching pathway in the design of iridium(III)-based phosphorogenic biomaterials for bioorthogonal labelling and imaging, Biomaterials 103 (2016) 305–313, https://doi.org/10.1016/j.biomaterials.2016.06.065.

[17] A.M.-H. Yip, K.K.-W. Lo, Luminescent rhenium(I), ruthenium(II), and iridium(III) polypyridine complexes containing a poly(ethylene glycol) pendant or bioorthogonal reaction group as biological probes and photocytotoxic agents, Coord. Chem. Rev. 361 (2018) 138–163, https://doi.org/10.1016/j.ccr.2018.01.021.

[18] T.S.-M. Tang, H.-W. Liu, K.K.-W. Lo, Monochromophoric iridium(III) pyridyl–tetrazine complexes as a unique design strategy for bioorthogonal probes with luminogenic behavior, Chem. Commun. 53 (2017) 3299–3302, https://doi.org/10.1039/C7CC00427C.

[19] P.K.-K. Leung, L.C.-C. Lee, H.H.-Y. Yeung, K.-W. Io, K.K.-W. Lo, Bioorthogonal control of the phosphorescence and singlet oxygen photosensitisation properties of iridium(III) tetrazine complexes, Chem. Commun. 57 (2021) 4914–4917, https://doi.org/10.1039/D1CC00545F.

[20] M. Schnierle, S. Blickle, V. Filippou, M.R. Ringenberg, Tetrazine metallation boosts rate and regioselectivity of inverse electron demand Diels–Alder (iEDDA) addition of dienophiles, Chem. Commun. 56 (2020) 12033–12036, https://doi.org/10.1039/D0CC03805A.

[21] A. Turlik, K.N. Houk, D. Svatunek, Origin of increased reactivity in rhenium-mediated cycloadditions of tetrazines, J. Org. Chem. 86 (2021) 13129–13133, https://doi.org/10.1021/acs.joc.1c01564.

[22] V.N. Kozhevnikov, M.E. Deary, T. Mantso, M.I. Panayiotidis, M.T. Sims, Iridium (III) complexes of 1,2,4-triazines as potential bioorthogonal reagents: metal coordination facilitates luminogenic reaction with strained cyclooctynes, Chem. Commun. 55 (2019) 14283–14286, https://doi.org/10.1039/C9CC06828G.

[23] M. Schnierle, M. Leimkühler, M.R. Ringenberg, [(η 6 - p- Cymene)[3-(pyrid-2-yl)-1,2,4,5-tetrazine]chlororuthenium(II)] +, redox noninnocence and dienophile addition to coordinated tetrazine, Inorg. Chem. 60 (2021) 6367–6374, https://doi.org/10.1021/acs.inorgchem.1c00094.

[24] M.G. Pfeffer, C. Müller, E.T.E. Kastl, A.K. Mengele, B. Bagemihl, S. Fauth, J. Habermehl, L. Petermann, M. Wächtler, M. Schulz, D. Chartrand, F. Laverdière, P. Seeber, S. Kupfer, S. Gräfe, G.S. Hanan, J.G. Vos, B. Dietzek, S. Rau, Active repair of a dinuclear photocatalyst for visible light-driven hydrogen production, Nat. Chem. Chem. (2022) https://doi.org/10.1038/s41557-021-00860-6 in print.

[25] K. Suzuki, A. Kobayashi, S. Kaneko, K. Takehira, T. Yoshihara, H. Ishida, Y. Shiina, S. Oishi, S. Tobita, Reevaluation of absolute luminescence quantum yields of standard solutions using a spectrometer with an integrating sphere and a back-thinned CCD detector, Phys. Chem. Chem. Phys. 11 (2009) 9850, https://doi.org/10.1039/b912178a.

[26] J. Kübel, R. Schroot, M. Wächtler, U.S. Schubert, B. Dietzek, M. Jäger, Photoredox-active dyads based on a Ru(II) photosensitizer equipped with electron donor or acceptor polymer chains: a spectroscopic study of light-induced processes toward efficient charge separation, J. Phys. Chem. C 119 (2015) 4742–4751, https://doi.org/10.1021/acs.jpcc.5b00866.

[27] R. Siebert, D. Akimov, M. Schmitt, A. Winter, U.S. Schubert, B. Dietzek, J. Popp, Spectroscopic investigation of the ultrafast photoinduced dynamics in π-conjugated terpyridines, ChemPhysChem 10 (2009) 910–919, https://doi.org/10.1002/cphc.200800847.

[28] C. Müller, T. Pascher, A. Eriksson, P. Chabera, J. Uhlig, KiMoPack – a python Package for Kinetic Modelling of Chemical Mechanism, J. Phys. Chem. A (2022) (2022), 10.1021/acs.jpca.2c00907 (accepted).

[29] A.L. Dobryakov, S.A. Kovalenko, N.P. Ernsting, Coherent and sequential contributions to femtosecond transient absorption spectra of a rhodamine dye in solution, J. Chem. Phys. 123 (2005), 044502, https://doi.org/10.1063/1.1948383.

[30] B. Dietzek, T. Pascher, V. Sundström, A. Yartsev, Appearance of coherent artifact signals in femtosecond transient absorption spectroscopy in dependence on detector design, Laser Phys. Lett. 4 (2007) 38–43, https://doi.org/10.1002/lapl.200610070.

[31] C. Ruckebusch, M. Sliwa, P. Pernot, A. de Juan, R. Tauler, Comprehensive data analysis of femtosecond transient absorption spectra: a review, J. Photochem. Photobiol. C Photochem. Rev. 13 (2012) 1–27, https://doi.org/10.1016/j.jphotochemrev.2011.10.002.

[32] J.E. Loefroth, Time-resolved emission spectra, decay-associated spectra, and species-associated spectra, J. Phys. Chem. 90 (1986) 1160–1168, https://doi.org/10.1021/j100278a040.

[33] J.M. Beechem, M. Ameloot, L. Brand, Global analysis of fluorescence decay surfaces: excited-state reactions, Chem. Phys. Lett. 120 (1985) 466–472, https://doi.org/10.1016/0009-2614(85)85642-6.

[34] J.M. Beechem, M. Ameloot, L. Brand, Global and Target analysis of complex decay phenomena, Instrum. Sci. Technol. 14 (1985) 379–402, https://doi.org/10.1080/10739148508543585.

[35] M.J. Frisch, G.W. Trucks, H.B. Schlegel, G.E. Scuseria, M.A. Robb, J.R. Cheeseman, G. Scalmani, V. Barone, G.A. Petersson, H. Nakatsuji, X. Li, M. Caricato, A. Marenich, J. Bloino, B.G. Janesko, R. Gomperts, B. Mennucci, H.P. Hratchia, D. J. Fox, Gaussian 16, Revision B.01, Gaussian, Inc., Wallingford CT, 2016.

[36] A.D. Becke, Density-functional thermochemistry. III. The role of exact exchange, J. Chem. Phys. 98 (1993) 5648–5652, https://doi.org/10.1063/1.464913.

[37] C. Lee, W. Yang, R.G. Parr, Development of the Colle-Salvetti correlation-energy formula into a functional of the electron density, Phys. Rev. B 37 (1988) 785–789, https://doi.org/10.1103/PhysRevB.37.785.

[38] F. Weigend, R. Ahlrichs, Balanced basis sets of split valence, triple zeta valence and quadruple zeta valence quality for H to Rn: design and assessment of accuracy, Phys. Chem. Chem. Phys. 7 (2005) 3297, https://doi.org/10.1039/b508541a.

[39] D. Andrae, U. Häußermann, M. Dolg, H. Stoll, H. Preuß, Energy-adjustedab initio pseudopotentials for the second and third row transition elements, Theor. Chim. Acta 77 (1990) 123–141, https://doi.org/10.1007/BF01114537.

[40] B. Mennucci, C. Cappelli, C.A. Guido, R. Cammi, J. Tomasi, Structures and properties of electronically excited chromophores in solution from the polarizable continuum model coupled to the time-dependent density functional theory, J. Phys. Chem. A 113 (2009) 3009–3020, https://doi.org/10.1021/jp8094853.

[41] A.V. Marenich, C.J. Cramer, D.G. Truhlar, Universal Solvation model based on solute electron density and on a continuum model of the solvent defined by the bulk dielectric constant and atomic surface tensions, J. Phys. Chem. B 113 (2009) 6378–6396, https://doi.org/10.1021/jp810292n.

[42] S. Grimme, S. Ehrlich, L. Goerigk, Effect of the damping function in dispersion corrected density functional theory, J. Comput. Chem. 32 (2011) 1456–1465, https://doi.org/10.1002/jcc.21759.

[43] S. Rau, B. Schäfer, A. Grüßing, S. Schebesta, K. Lamm, J. Vieth, H. Görls, D. Walther, M. Rudolph, U.W. Grummt, E. Birkner, Efficient synthesis of ruthenium complexes of the type (R-bpy)2RuCl2 and [(R-bpy)2Ru(L–L)]Cl2 by microwave-activated reactions (R: H, Me, tert-But) (L–L: substituted bibenzimidazoles, bipyrimidine, and phenanthroline), Inorg. Chim. Acta 357 (2004) 4496–4503, https://doi.org/10.1016/j.ica.2004.07.007.

[44] O.A. Lenis-Rojas, A.R. Fernandes, C. Roma-Rodrigues, P.V. Baptista, F. Marques, D. Pérez-Fernández, J. Guerra-Varela, L. Sánchez, D. Vázquez-García, M.L. Torres, A. Fernández, J.J. Fernández, Heteroleptic mononuclear compounds of ruthenium (II): synthesis, structural analyses, in vitro antitumor activity and in vivo toxicity on zebrafish embryos, Dalton Trans. 45 (2016) 19127–19140, https://doi.org/10.1039/C6DT03591D.

[45] R. Staehle, C. Reichardt, J. Popp, D. Sorsche, L. Petermann, K. Kastner, C. Streb, B. Dietzek, S. Rau, Ruthenium imidazophenanthrolinium complexes with prolonged excited-state lifetimes, Eur. J. Inorg. Chem. 2015 (2015) 3932–3939, https://doi.org/10.1002/ejic.201500021.

[46] G. Cooke, G.M. Ó Máille, R. Quesada, L. Wang, S. Varughese, S.M. Draper, Substituted pyridazines as ligands in homoleptic (fac and mer) and heteroleptic Ru (ii) complexes, Dalton Trans. 40 (2011) 8206, https://doi.org/10.1039/c1dt10340g.

[47] M. Schwalbe, B. Schäfer, H. Görls, S. Rau, S. Tschierlei, M. Schmitt, J. Popp, G. Vaughan, W. Henry, J.G. Vos, Synthesis and characterisation of poly(bipyridine) ruthenium complexes as building blocks for heterosupramolecular arrays, Eur. J. Inorg. Chem. 2008 (2008) 3310–3319, https://doi.org/10.1002/ejic.200701303.

[48] B. Sarkar, R.H. Laye, B. Mondal, S. Chakraborty, R.L. Paul, J.C. Jeffery, V. G. Puranik, M.D. Ward, G. Kumar Lahiri, Synthesis, structure and spectroelectrochemical properties of a dinuclear ruthenium complex exhibiting a strong electronic interaction across a 1,2,4,5-tetrazine bridging ligand, J. Chem. Soc. Dalton Trans. (2002) 2097–2101, https://doi.org/10.1039/b108296e.

[49] T. Troll, Reduction potentials of substituted as-triazines and s-tetrazines in acetonitrile, Electrochim. Acta. 27 (1982) 1311–1314, https://doi.org/10.1016/0013-4686(82)80153-9.

[50] J.E.B. Johnson, C. de Groff, R.R. Ruminski, Synthesis and characterization of tetraammineruthenium(II) complexes bound to the bridging ligand 3,6-bis(2-pyridyl)1,2,4,5-tetrazine (bptz): comparative effects of σ and π peripheral ligands on electronic absorption and electrochemical properties, Inorg. Chim. Acta. 187 (1991) 73–80, https://doi.org/10.1016/S0020-1693(00)82979-5.

[51] S.D. Ernst, W. Kaim, Energy level tailoring in ruthenium(II) polyazine complexes based on calculated and experimental ligand properties, Inorg. Chem. 28 (1989) 1520–1528, https://doi.org/10.1021/ic00307a020.

[52] D. Pandiarajan, R. Ramesh, µ-Halo bridged binuclear ruthenium(III) complexes featuring pyridazine ligands: synthesis, structure, spectral and electrochemical properties, Polyhedron 34 (2012) 136–142, https://doi.org/10.1016/j.poly.2011.12.035.

[53] S. Ghumaan, B. Sarkar, S. Patra, K. Parimal, J. van Slageren, J. Fiedler, W. Kaim, G. K. Lahiri, 3,6-Bis(2′-pyridyl)pyridazine (L) and its deprotonated form (L – H +) – as ligands for {(acac) 2 Ru n+} or {(bpy) 2 Ru m+}: investigation of mixed valency in [{(acac) 2 Ru} 2 (µ-L – H +)] 0 and [{(bpy) 2 Ru} 2 (µ-L – H +)] 4+ by spectroelectrochemist, Dalton Trans. (2005) 706–712, https://doi.org/10.1039/B417530A.

[54] A. Nayak, S. Patra, B. Sarkar, S. Ghumaan, V.G. Puranik, W. Kaim, G.K. Lahiri, Tetrazine derived mononuclear RuII(acac)2(L) (1), [RuII(bpy)2(L)](ClO4)2 (2) and [RuII(bpy)(L)2](ClO4)2 (3) (L=3-amino-6-(3,5-dimethylpyrazol-1-yl)-1,2,4,5-tetrazine, acac=acetylacetonate, bpy=2,2′-bipyridine): syntheses, structures, spectra and redox pro, Polyhedron 24 (2005) 333–342, https://doi.org/10.1016/j.poly.2004.11.019.

[55] M. Kasha, Characterization of electronic transitions in complex molecules, Discuss. Faraday Soc. 9 (1950) 14, https://doi.org/10.1039/df9500900014.

[56] R. Englman, J. Jortner, The energy gap law for radiationless transitions in large molecules, Mol. Phys. 18 (1970) 145–164, https://doi.org/10.1080/00268977000100171.

[57] J.V. Caspar, E.M. Kober, B.P. Sullivan, T.J. Meyer, Application of the energy gap law to the decay of charge-transfer excited states, J. Am. Chem. Soc. 104 (1982) 630–632, https://doi.org/10.1021/ja00366a051.

[58] K.K.-W. Lo, Luminescent rhenium(I) and Iridium(III) polypyridine complexes as biological probes, imaging reagents, and photocytotoxic agents, Acc. Chem. Res. 48 (2015) 2985–2995, https://doi.org/10.1021/acs.accounts.5b00211.

[59] A. Juris, V. Balzani, F. Barigelletti, S. Campagna, P. Belser, A. von Zelewsky, Ru(II) polypyridine complexes: photophysics, photochemistry, eletrochemistry, and chemiluminescence, Coord. Chem. Rev. 84 (1988) 85–277, https://doi.org/10.1016/0010-8545(88)80032-8.

[60] C.W. Stark, W.J. Schreier, J. Lucon, E. Edwards, T. Douglas, B. Kohler, Interligand electron transfer in heteroleptic ruthenium(II) complexes occurs on multiple time scales, J. Phys. Chem. A 119 (2015) 4813–4824, https://doi.org/10.1021/acs.jpca.5b01770.

[61] S. Wallin, J. Davidsson, J. Modin, L. Hammarström, Femtosecond transient absorption anisotropy study on [Ru(bpy) 3] 2+ and [Ru(bpy)(py) 4] 2+ . ultrafast interligand randomization of the MLCT state, J. Phys. Chem. A 109 (2005) 4697–4704, https://doi.org/10.1021/jp0509212.

[62] J.K. McCusker, Femtosecond absorption spectroscopy of transition metal charge-transfer complexes, Acc. Chem. Res. 36 (2003) 876–887, https://doi.org/10.1021/ar030111d.

[63] N.H. Damrauer, G. Cerullo, A. Yeh, T.R. Boussie, C.V. Shank, J.K. McCusker, Femtosecond dynamics of excited-state evolution in [Ru(bpy) 3] 2+, Science 275 (1997) 54–57, https://doi.org/10.1126/science.275.5296.54, 80-.

[64] J. Yuasa, S. Fukuzumi, Mechanistic borderline between one-step hydrogen transfer and sequential transfers of electron and proton in reactions of NADH analogues with triplet excited states of tetrazines and Ru(bpy) 3 2+*, J. Am. Chem. Soc. 128 (2006) 14281–14292, https://doi.org/10.1021/ja0604562.

[65] J. Yuasa, S. Fukuzumi, Remarkable oxidizing ability of triplet excited states of tetrazines produced by photosensitization with Ru(bpy) 3 2+, Chem. Commun. (2006) 561–563, https://doi.org/10.1039/B513110C.

[66] A.K. Mengele, C. Müller, D. Nauroozi, S. Kupfer, B. Dietzek, S. Rau, Molecular scylla and charybdis: maneuvering between pH sensitivity and excited-state localization in ruthenium Bi(benz)imidazole complexes, Inorg. Chem. 59 (2020) 12097–12110, https://doi.org/10.1021/acs.inorgchem.0c01022.

[67] N.H. Damrauer, G. Cerullo, A. Yeh, T.R. Boussie, C.V. Shank, J.K. McCusker, Femtosecond dynamics of excited-state evolution in [Ru(bpy)3]2+, Science 275 (1997) 54–57, https://doi.org/10.1126/science.275.5296.54, 80-.

[68] C. Kreitner, E. Erdmann, W.W. Seidel, K. Heinze, Understanding the excited state behavior of cyclometalated bis(tridentate)ruthenium(II) Complexes: a combined experimental and theoretical study, Inorg. Chem. 54 (2015) 11088–11104, https://doi.org/10.1021/acs.inorgchem.5b01151.

[69] D.G. Brown, N. Sanguantrakun, B. Schulze, U.S. Schubert, C.P. Berlinguette, Bis (tridentate) ruthenium–terpyridine complexes featuring microsecond excited-state lifetimes, J. Am. Chem. Soc. 134 (2012) 12354–12357, https://doi.org/10.1021/ja3039536.

[70] N.A. Kuznetsova, N.S. Gretsova, O.A. Yuzhakova, V.M. Negrimovskii, O.L. Kaliya, E.A. Luk'yanets, New reagents for determination of the quantum efficiency of singlet oxygen generation in aqueous media, Russ. J. Gen. Chem. (2001) 36–41, https://doi.org/10.1023/A:1012369120376.

[71] S.M. Mooi, B. Heyne, Amplified production of singlet oxygen in aqueous solution using metal enhancement effects, Photochem. Photobiol. 90 (2014) 85–91, https://doi.org/10.1111/php.12176.

[72] D. Garcìa-Fresnadillo, Y. Georgiadou, G. Orellana, A.M. Braun, E. Oliveros, Singlet-Oxygen (1 Δg) Production by Ruthenium(II) complexes containing polyazaheterocyclic ligands in methanol and in water, Helv. Chim. Acta 79 (1996) 1222–1238, https://doi.org/10.1002/hlca.19960790428.

[73] M. DeRosa, Photosensitized singlet oxygen and its applications, Coord. Chem. Rev. 233–234 (2002) 351–371, https://doi.org/10.1016/S0010-8545(02)00034-6.